PAPER

Check for updates

Rationalizing the interphase stability of Li|doped-Li₇La₃Zr₂O₁₂ *via* automated reaction screening and machine learning†

Bo Liu,[ab] Jiong Yang, ID *[a] Hongliang Yang,[bc] Caichao Ye,[b] Yuanqing Mao,[b] Jiping Wang,[b] Siqi Shi, ID [a] Jihui Yang ID *[d] and Wenqing Zhang*[b]

Lithium metal batteries are a promising candidate for future high-energy-density energy storage. However, dendrite growth and the high reactivity of the Li metal anode result in low cycling efficiency and severe safety concerns. Here, we present a strategy to stabilize the lithium metal anode through cation doping in $Li_7La_3Zr_2O_{12}$ (LLZOM, M = dopant). High-throughput automated reaction screening together with a machine learning approach are developed to evaluate possible reactions and the thermodynamic stability of the Li|LLZOM interfaces under various chemical conditions. It is discovered that some dopants, such as M = Sc^{3+} (doping on Zr site), Ce^{3+} (La or Zr), Ac^{3+} (La), Y^{3+} (La or Zr), Tm^{3+} (La or Zr), Er^{3+} (La or Zr), Ho^{3+} (La or Zr), Dy^{3+} (La or Zr), Nd^{3+} (La or Zr), Tb^{3+} (La or Zr), Pr^{3+} (La), Pm^{3+} (La or Zr), Sm^{3+} (La or Zr), Gd^{3+} (La or Zr), Lu^{3+} (La), Ce^{4+} (Zr), Th^{4+} (Zr), and Pa^{5+} (Zr), exhibit thermodynamic stability against Li; while others, M = Ca^{2+} (La or Zr), Yb^{3+} (La), Br^{3+} (Li), Te^{4+} (Zr), Se^{4+} (Zr), S^{4+} (Zr), Hf^{4+} (Zr), Cl^{5+} (Zr), and I^{5+} (Zr), may lead to the spontaneous formation of a stable, passivating solid electrolyte interphase (SEI) layer on the Li metal, and alleviate dendritic lithium growth. From the machine learning approach, the formation energy of oxides M_xO_y emerges as the most crucial feature dominating the route of interface reactions, implying that the M−O bond strength governs the interface stability of the cation-doped LLZOM. The machine learning model then predicts 18 unexplored LLZOM systems, which are all validated in subsequent calculations. Our work offers practical insights for experimentalists into the selection of appropriate dopants in LLZO to stabilize Li metal anodes in solid-state batteries.

Introduction

Lithium (Li) metal is an ideal anode material for next-generation high-energy- and high-power-density batteries owing to its extremely high theoretical specific capacity (3860 mA h g⁻¹), low density (0.59 g cm⁻³ at room temperature), and the lowest negative electrochemical potential (−3.040 V *vs.* H/H⁺).[1–3] Enabling Li metal anode has been regarded as the "Holy Grail" and is confronted by many challenges. Li dendrite formation and propagation, and Li anode pulverization in liquid electrolytes cause poor cycling performance, low coulombic efficiency, and severe safety concerns during battery cycling, which have hampered the practical

applications of the Li metal anode over the past decades.[4,5] Solid-state electrolytes (SSEs) are a potential solution to these issues inherent to Li metal. Ideal SSE materials should possess high Li⁺ conductivity (*e.g.*, >10⁻⁴ S cm⁻¹ at room temperature), be electrically insulating, have a wide electrochemical window (*e.g.*, >6 V *vs.* Li⁺/Li), possess stability against both electrodes and moisture, *etc.*[6] One major challenge in developing solid-state batteries stems from the lack of understanding of electrode–SSEs interfacial stability, specifically the Li metal–SSEs interface.[7,8] To prevent the reduction of Li metal, SSEs that are thermodynamically stable or that form stable passivation layers against Li metal are needed. The state-of-the-art SSE materials, including sulfides ($Li_{10}GeP_2S_{12}$ (ref. 9) and $Li_7P_3S_{11}$ (ref. 10)), oxynitrides (LiPON[11]), perovskite ($Li_{0.33}La_{0.56}TiO_3$ (ref. 12)), and NASICON-type ($Li_{1.3}Al_{0.3}Ti_{1.7}(PO_4)_3$ (ref. 13) and $LiZr_2(PO_4)_3$ (ref. 14)), can be reduced to form a solid electrolyte interphase (SEI) layer at the interface once in contact with the Li metal anode. If the SEI layer is electrically insulating, it passivates the SSE materials against further Li reduction, which is critical to achieve good stability.[15] Among various SSE materials, the garnet-type $Li_7La_3Zr_2O_{12}$ (LLZO) has drawn much attention because of its high Li⁺ conductivity at room

[a]*Materials Genome Institute, Shanghai University, Shanghai 200444, China*

[b]*Department of Physics, Shenzhen Institute for Quantum Science & Technology, Southern University of Science and Technology, Shenzhen, Guangdong 518055, China*

[c]*State Key Laboratory of High Performance Ceramics and Superfine Microstructure, Shanghai Institute of Ceramics, Chinese Academy of Sciences, Shanghai 200050, China*

[d]*Department of Materials Science and Engineering, University of Washington, Seattle, WA 98195, USA. E-mail: jiongy@t.shu.edu.cn; zhangwq@sustc.edu.cn; jihuiy@uw.edu*

This journal is © The Royal Society of Chemistry 2019

J. Mater. Chem. A, 2019, 7, 19961–19969 | **19961**

temperature (10^{-3} to 10^{-4} S cm^{-1}) and reasonable electro-chemical stability against Li metal.[16–19]

It has been reported that cation doping in cubic LLZO, such as Nb^{5+}, Ta^{5+}, W^{6+}, or Mo^{6+} substituting for Zr^{4+},[20–23] as well as Al^{3+} or Ga^{3+} for the Li sublattice,[24,25] affects the cubic phase stability and increases the ionic conductivity. It was worth noting that the thermodynamic stability of the Li|LLZO interface is also affected by the doped cations. Nemori et al.[26] and Kim et al.[27] reported that Ta^{5+}-doped LLZO samples are stable in contact with Li, whereas those with Nb^{5+} are not. Ma et al.[28] investigated the reactions at the Li|cubic-Li$_{7-3x}$Al$_x$-La$_3$Zr$_2$O$_{12}$ (c-LLZO) interface, which forms a tetragonal-like LLZO interphase with 6 nm thickness, possibly inhibiting further chemical reactions. D. Rettenwander et al.[29] reported that Li$_{6.4}$Fe$_{0.2}$La$_3$Zr$_2$O$_{12}$, even with a high total conductivity of 1.1 mS cm^{-1} at room temperature, is not stable against Li metal and forms a thick tetragonal LLZO interlayer, causing high interfacial resistance. Nakayama et al.[18] used density functional theory (DFT) to investigate the electrochemical stability of different garnets with the composition Li$_x$La$_3$-M$_2$O$_{12}$ ($x = 5$ or 7; M = Ti, Zr, Nb, Ta, Sb, Bi) against Li metal and found that the electrochemical stability is strongly dependent on the effective charge states of the M cations. Moreover, a surface-science-based approach was used to successfully identify the reduction of different dopant species (Nb, Ta, and Al) in LLZO samples by Li metal, suggesting that dopants do indeed play a critical role in determining the reactivity of the Li|LLZO interface.[30,31] This leads to the hypothesis that the thermodynamic stability against Li metal of LLZO can be regulated by cation doping, which needs further validation.

So far, there has not been any systematic study on whether the cation doping of LLZO (labeled as LLZOM) improves its stability against Li metal. Owing to the lack of knowledge on the stability and composition-dependent reactions of LLZOM in contact with Li metal, prior studies on screening for appropriate dopants are mostly based on the trial-and-error approach. A predictive model for the thermodynamic stability of cation-doped LLZOM against Li metal is necessary. The present study is motivated by two fundamental questions. First, which cation dopant in LLZO is beneficial to the thermodynamic stability against Li metal? Second, what factors dominate the stability of Li|LLZOM interfaces?

In this paper, by using a first-principles approach based on a large-scale materials database, we build an automated route to screen all possible reactions corresponding to LLZOM in contact with varying amounts of Li, and to calculate the reaction energies ($\Delta G_{\text{LLZOM–Li}}$) for the formation of the lowest-energy phases. We also obtain a machine learning model for classifying Li|LLZOM interfaces as thermodynamically stable or unstable with high accuracy. Our results reveal that the thermodynamic stability of LLZOM against Li metal can be improved when the dopant–oxygen bond in LLZOM is strong. By applying our machine learning model, 18 unexplored dopants M in LLZOM systems against Li metal are predicted and further validated in our automated calculations.

Methods

Formation energy calculations

In general, the formation energy for a compound is given by[32]

$$\Delta H_f = E_{\text{tot}} - \sum_i \mu_i x_i, \tag{1}$$

where E_{tot} is the DFT total energy of the compound, μ_i is the chemical potential of element i, and x_i is quantity of element i in the compound, respectively. As suggested by ref. 32, the DFT total energy of the elemental substance can be used as the chemical potential of each species. Strictly speaking, the computed formation energy is valid only for 0 K.

Phase stability calculations

The energy above the convex hull (E_{hull}) of each LLZOM compound was evaluated using pymatgen based on the DFT energies.[33] Stable compounds have an E_{hull} value of 0 eV per atom, and higher values indicate increasing metastability.

First-principles calculations

Density functional theory (DFT) calculations were performed within the generalized gradient approximation (GGA) with the Perdew, Burke and Ernzerhof (PBE) exchange–correlation functional,[34] using a plane wave basis set and the projector augmented wave (PAW) method[35] as implemented in the Vienna Ab initio Simulation Package (VASP) code.[36] Energy cutoff for the plane waves was set to be 520 eV. The convergence thresholds for self-consistency and forces were 10^{-5} eV and 10^{-2} eV Å^{-1}, respectively. The DFT+U was used to accurately describe the transition metal (Co, Cr, Fe, Mn, Mo, Ni, V, and W) for the strong correlation of d-electrons, and the U values were chosen with reference to the Materials Project (MP) database.[33] The energy correction for anions, transition metals, and gas/liquid phase was included in the MP database.[33] For pristine LLZO cells, we used an eight formula units conventional supercell, with cubic symmetry group $Ia\bar{3}d$. Li was distributed on the partially occupied 24d and 96h sites by using an electrostatic energy criterion that excluded occupation of electrostatically unfavorable first nearest-neighbor sites.[37] Before calculating the properties of doped LLZO, we compared the total energies of several pristine LLZO cells containing different distributions of Li ions across the available Li sites. The structure having the lowest total energy from this set of candidates was adopted for subsequent calculations.

Machine learning method

Support vector machine (SVM) classification. For the SVM classification problem, each instance of our data is described by an n-dimensional feature vector $\vec{x} = (f_1, f_2, f_3, \ldots, f_n)$ and a target label y. The label has a value of +1, say, for thermodynamically stable, and −1, for unstable. An SVM aims to find a function that for any given $\vec{x}$ has a value of ±1. Ideally, it is desired to generate a decision boundary in the space of features that maximizes the distance (also known as margin) of the closest instance of either class from it. Instances are defined as points

19962 | J. Mater. Chem. A, 2019, **7**, 19961–19969

This journal is © The Royal Society of Chemistry 2019

in the hyperspace of features that lie on one side or the other of this hypersurface. If we represent our input data by the set of label distances $\{(\vec{x}_i, y_i)\}$, then a soft margin support vector classifier determines the hypersurface in the space of features by solving

$$\alpha_1, \ldots, \alpha_n = \text{argmin} - \frac{1}{2} \sum_{i=1}^{m} \sum_{j=1}^{m} \alpha_i \alpha_j \kappa(\vec{x}_i, \vec{x}_j) + \sum_{i=1}^{m} \alpha_i, \quad (2)$$

subject to the following constraints

$$0 \leq \alpha_i \leq C \text{ and } \sum_{i=1}^{m} \alpha_i y_i = 0. \quad (3)$$

The kernel $\kappa(\vec{x}_i, \vec{x}_j)$ has linear kernels, polynomial kernels, or Gaussian kernels (radial *basis* function kernels, RBFs). In this work, however, after testing a number of kernels for their classification accuracies, we chose to go forward with a Gaussian kernel, defined as

$$\kappa(\vec{x}_i, \vec{x}_j) = \exp(-\gamma |\vec{x}_i - \vec{x}_j|^2). \quad (4)$$

Kernel ridge regression (KRR). Within the KRR model, the reaction energy of a system in the test set is given by a sum of a weighted Laplacian over the entire training set. As a part of the model training process, the learning is performed by minimizing the expression

$$\sum_{i=1}^{N} \left(G_{\text{KRR}}^{i} - G_{\text{DFT}}^{i} \right)^2 + \lambda \sum_{i=1}^{N} \omega_i^2, \quad (5)$$

with G_{KRR}^{i} being the KRR estimated reaction energy value, G_{DFT}^{i} the DFT value, and λ a regularization parameter. The explicit solution to this minimization problem is $\omega = (k + \lambda I)^{-1} G_{\text{DFT}}$,
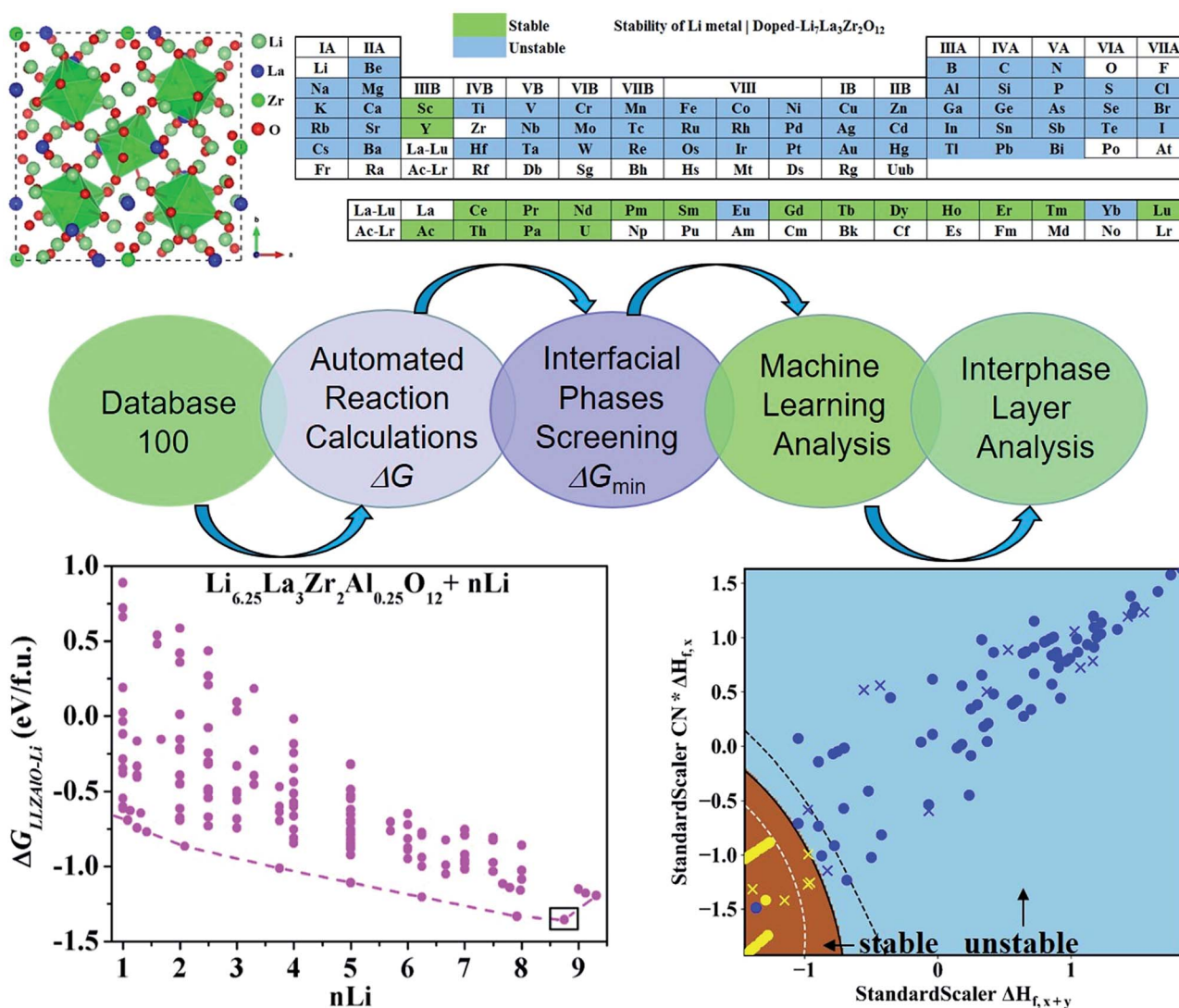

Fig. 1 The workflow of the automated interface reaction screening process and machine learning to efficiently search for cation-doped LLZO thermodynamically stable against Li metal used in LLZO-based all-solid batteries. The atomic structure, automated interface reaction screening, dopant screening, and interface stability machine learning classification results are presented.

where I is the identity matrix, and the kernel $\kappa(\vec{x}_i, \vec{x}_j)$ has linear kernels, polynomial kernels, Gaussian kernels (RBFs), or Laplacian kernels. In this work, however, after testing a number of kernels for their classification accuracies, we chose to go forward with a Laplacian kernel, defined as

$$K(\vec{x}_i, \vec{x}_j) = \exp\left(-\frac{1}{\sigma}|\vec{x}_i - \vec{x}_j|\right). \qquad (6)$$

The parameters λ, σ are determined in an inner loop of five-fold cross-validation using a logarithmically scaled fine grid.

The coefficient of determination (R^2), employed to evaluate the model accuracy, is defined as

$$R^2 = 1 - \frac{\sum_i \left(y_i^{\text{true}} - y_i^{\text{pred}}\right)^2}{\sum_i (y_i^{\text{true}} - y_i^{-\text{true}})^2}, \qquad (7)$$

where y is the reaction energy value. The closer to 1 is the value of R^2, the better the fit of predicted values to the regression line. The mean squared error (MSE) represents the mean difference between the predicted values and the real values, defined as

$$\text{MSE} = \frac{1}{N}\sum_i^N |y_i^{\text{true}} - y_i^{\text{pred}}|. \qquad (8)$$

Results and discussion

Automated reaction screening for possible interphases

To find the optimal cation doping in LLZO that can be stable against Li metal, we construct a screening workflow as illustrated in Fig. 1. First, a database containing the identities and formation energies of all of the relevant material phases, including the LLZOM phase and the product phases, is created, corresponding to more than 100 LLZOM structures which cover the Li-site, La-site, and Zr-site doping. For all calculations, we employ similar parameters, *e.g.*, the cutoff energy of plane waves, convergence criterion, *etc.*, in order to make all data comparable. The phase stability of the single phase LLZOM can be estimated by determining its E_{hull} value in the relevant multicomponent phase diagram. As shown in Fig. S1b,† each LLZOM has relatively small energy above the hull, suggesting that it has good phase stability. For each LLZOM reaction with Li metal, all possible product phases, including ternary compounds (Li–O–Zr, Li–O–M, La–Zr–O, La–M–O), binary compounds (Li–O, Zr–O, La–O, M–O, Zr–M), and simple substances (Zr, M) are considered. The structures and formation energies (ΔH_{f}) of the product phases are taken from the Materials Project (MP) database.[33] We compare the corresponding $\Delta H_{\text{f}}^{\text{DFT}}$ (ref. 33) and $\Delta H_{\text{f}}^{\text{exp}}$ (ref. 38 and 39) values of some product phases in Fig. S2.† The difference between the $\Delta H_{\text{f}}^{\text{DFT}}$ and $\Delta H_{\text{f}}^{\text{exp}}$ is relatively small, which implies DFT calculations can provide an acceptable level of accuracy in formation energy of product phases. Nevertheless, the reactant LLZOM has no matching entry with formation energies in MP; instead, a convex hull energy of LLZOM is used for reaction energy calculation. Herein, the formation energies of the LLZOM are

calculated by DFT directly, which can increase the accuracy of the calculations for Li|LLZOM reactions. The possible reaction equations of LLZOM in contact with Li metal are constructed by an automatic reaction balance procedure. The high-throughput calculation framework used here relies on the availability of accurate formation energies to calculate the reaction energies of the Li|LLZOM interfaces, once the database is compiled.

From the large amount of calculated reaction energies data, the reactions with the lowest reaction energies are selected to be the most possible interphase reactions corresponding to the equilibrium product phases. This is a fully automated prediction of the product phases with different reactants. As a result, only the reaction-forming phase with the lowest reaction energy is adopted for further interface stability evaluations. The final thermodynamic stability of a specific Li|LLZOM interface is determined by whether the two materials have an exothermic reaction to form other phases. We calculate the reaction energies of LLZOM with metallic Li by reduction, according to the following equations

$$n\text{Li} + \text{LLZOM} \rightarrow \text{product phases}, \qquad (9)$$

$$\Delta G_{\text{LLZOM–Li}} = E\,[\text{product phases}] - E\,[\text{LLZOM}] - nE\,[\text{Li}], (10)$$

where the reaction energy $\Delta G_{\text{LLZOM–Li}}$ is the thermodynamic driving force for reactions between the LLZOM and Li, E [product phases] represents the formation energies of the product phases, and E [LLZOM] and E [Li] are the formation energies of the LLZOM and metallic lithium, respectively. Based on the calculated $\Delta G_{\text{LLZOM–Li}}$, Li|LLZOM reactions can be classified into two categories: (i) $\Delta G_{\text{LLZOM–Li}} > 0$, LLZOM phase in contact with Li is thermodynamically stable, namely, LLZOM and Li do not react with each other to form other phases in reduction processes; (ii) $\Delta G_{\text{LLZOM–Li}} < 0$, LLZOM phase is thermodynamically unstable, reacting with Li to form an interphase layer with various phases. All data about the formation energies of the LLZOM, reaction energies and product phases between Li metal and LLZOM compounds can be found in Table S1.† We further extract the reduction behavior of different doped systems and analyze the determining factors of cation doping on the stability of LLZO against Li metal by a machine learning approach. The formation energy of oxides M_xO_y, together with other feature factors, governs the stability of the Li|LLZOM interface. Furthermore, data analysis and visualization are performed to unravel the hidden trends. Given that a reasonable ionic conductivity is the precondition for solid electrolyte applications, we also perform bond-valence site energy (BVSE) calculations to evaluate the energy barriers of Li ion migration in each of the LLZOM compounds using our developed BVSE program,[40–42] and estimate the diffusion coefficient D by the equation $D = \nu a^2 \exp(-E_a/k_B T)$, as listed in Table S2.† The results show that high-valent dopants have an increasing trend in ionic conductivity, which is consistent with previous reports.[20–25]

As mentioned above, a successful workflow of the optimal dopant screening, including high-throughput interface reaction calculations and machine learning prediction, has been

19964 | *J. Mater. Chem. A*, 2019, **7**, 19961–19969

This journal is © The Royal Society of Chemistry 2019

demonstrated. For the high-throughput automated reaction calculations, using the Al-doped LLZO system as an example in Fig. 1 (bottom panels), only the reactions with the lowest reaction energies (bottom left panel), along the dashed line, represent the most likely decomposition path, *i.e.* the lithiation reaction of $Li_{7-x}La_3Zr_2Al_xO_{12}$ ($x = 0.25$). Fig. 2a shows that the reaction path starts with the product phases of La_2O_3, Li_5AlO_4, $Li_6Zr_2O_7$, and $ZrAl_3$; and eventually forms La_2O_3, Li_2O, Zr_4O, and Zr_3Al. The final product phases (La_2O_3, Li_2O, Zr_4O, and Zr_3Al) have a reaction energy of -1.244 eV per formula unit (f.u.). Fig. 2b shows the reaction energy for different dopant contents ($Li_{7-x}La_3Zr_2Al_xO_{12}$ with $x = 0.125$, 0.25). Overall, the reaction energy increases greatly with decreasing Al concentration, *e.g.*, as Al concentration decreases to 0.125, the reaction energy of the final product phases becomes -0.039 eV per formula unit. The results suggest that the thermodynamic stability of LLZOM against Li metal can be improved by controlling the dopant M contents. Higher M doping concentrations will cause instability of the Li|LLZOM interface (see ESI Fig. S3†).

M–O bond-strength-related interphase stability from data mining

In this section, we try to adopt the data mining technique to reveal the underlying mechanism of interfacial stability. Advanced machine learning methods become more and more important in the field of data mining as they have the potential to solve many complex problems, including prediction of physical properties and crystal structures, and uncover the physical mechanisms using a large amount of data from either high-throughput computation or experiments.[43–49] The key steps of data mining for the thermodynamic stability analysis of the Li|LLZOM interfaces are the selection of features (or descriptors) and the choice of model for machine learning algorithms.

The site and valence state for possible Li-, La-, and Zr-site dopants in LLZO, after filtering with a defect energy cutoff of 2 eV, are computed by DFT following previous work.[50] By applying this filter, the dataset for machine learning can be expanded. The dataset for this study comprises 100 LLZOM compounds, mainly from our own DFT calculations. The

reaction data, *i.e.*, the reaction equation and reaction energy for each LLZOM against Li metal, are analyzed using an automatic reaction screening process. The Li|LLZOM interface is labeled ± 1, with label $+1$ for a thermodynamically stable phase and label -1 for a thermodynamically unstable one. Typically, features are properties of a material that can distinguish one compound from others.[46,49,51] In our study, since the doping elements are different in LLZOM, we consider many relevant properties of the doping element as the features. Fifteen features for each LLZOM compound are selected for the machine learning procedure. They are: (i) valence states (VS) of dopant element M; (ii) ionic radius (r^i_M) and atomic radius (r^c_M) of element M from Shannon's work,[52] adopting the values under the same coordination number (CN) in LLZOM; (iii) atomic mass (AM) of element M; (iv) Pauling electronegativity (χ_M) of element M; (v) first ionization energy ($1^{st}IE_M$) of element M; (vi) the formation energy per atom defined as $\Delta H_{f,x+y} = \Delta H_f/(x+y)$, where ΔH_f is the heat for formation of the formula M_xO_y, the experimental formation energies from the SGTE Solid SUBstance (SSUB) database[39] and the thermodynamic database at the Thermal Processing Technology Center at the Illinois Institute of Technology (IIT),[38] and calculation formation energies from the MP database (see Table S3†). The majority of the calculated ΔH_f values are consistent with the measured data within ± 0.2 eV per atom, with a few exceptions. (vii) Oxygen coordination number (CN) of dopant element M in LLZO; (viii) product of coordination number CN with the formation energy of oxide M_xO_y per M atom ($CN \times \Delta H_{f,x}$), and product of coordination number CN with the formation energy of oxide M_xO_y per oxygen atom ($CN \times \Delta H_{f,y}$), where $\Delta H_{f,x} = \Delta H_f/x$ and $\Delta H_{f,y} = \Delta H_f/y$. The parameters $CN \times \Delta H_{f,x}$ and $CN \times \Delta H_{f,y}$ can be possibly viewed as the effective measurement of local interaction strength with dopant M in LLZO. (ix) Ratio of M ionic radius to O ionic radius, denoted as r^i_M/r^i_O; (x) electron configurations of $s + p$, d and f orbitals of dopant element M; and (xi) bond dissociation energies (BDE) of M–O from the *Handbook of Chemical Bond Energies* (see Table S4†).[53] The random forest classifier in scikit-learn package[54] is adopted to measure the importance of the features by calculating their weights. As shown in Fig. 3, the formation energy ($\Delta H_{f,x+y}$) plays the most
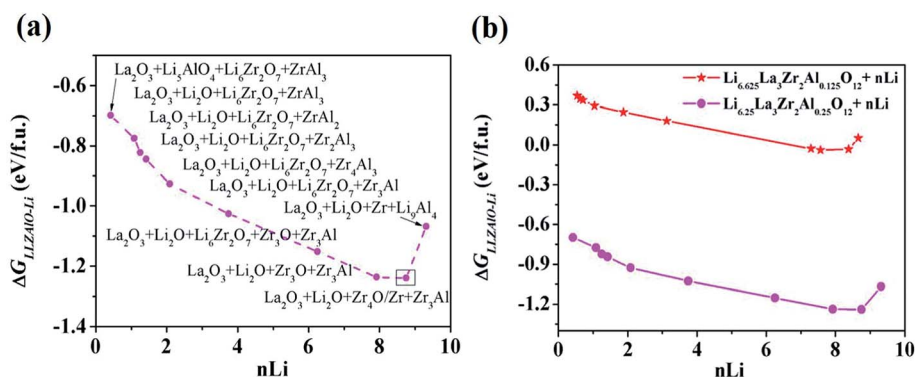

Fig. 2 The thermodynamic stability of LLZOAl when it reacts with Li. (a) The reaction paths and product phases along the dashed lines are marked, and the lowest reaction energy is marked with a square. (b) The reaction energy of the Li|LLZOAl interface *vs.* the doping concentration.

Fig. 3 The importance of the selected features. The 15 selected features are ranked using a random forest algorithm.

important role in determining the thermodynamic stability of LLZOM against Li, followed by the local interaction of M (CN × $\Delta H_{f,x}$, CN × $\Delta H_{f,y}$), the electronegativity (χ_M), and M–O bond dissociation energies (BDE). Pearson correlation coefficient (P) matrices are also calculated to identify the positive and negative correlations between pairs of features in Fig. S4.†

In our work, we adopt the machine learning technique in two different ways: (i) as a binary classification problem, where the machine should simple predict if the Li|LLZOM interface is thermodynamically stable (label 1) or not (label −1), and (ii) as a regression problem, where the machine predicts the reaction energy for the Li|LLZOM interface. In both situations, we adopt the machine learning model with best performance.[48] For example, five different classification algorithms, including logistic regression, support vector machine (SVM), decision

tree, extra tree, and neural network, are adopted. Each classification algorithm is fitted using the training data with two, three, four, or even more features at a time. The SVM with Gaussian kernel algorithm is found to be the most effective model based on the five-fold cross-validation results, and the performance of the top five feature pairs is summarized in ESI Table S5.† The best feature pair is ($\Delta H_{f,x+y}$, CN × $\Delta H_{f,x}$), with both accuracy and F_1 score of 0.99(±0.02) for the test set. It is worth noting that all the five top-performing feature pairs contain $\Delta H_{f,x+y}$. Going beyond two features does not improve the model performance, so we use our best performing model (SVM) with two features for subsequent analyses and predictions.

The maps of the best feature pairs, *i.e.*, ($\Delta H_{f,x+y}$, CN × $\Delta H_{f,x}$) and ($\Delta H_{f,x+y}$, BDE), are shown in Fig. 4a and b, with yellow circles indicating thermodynamically stable ($\Delta G_{LLZOM-Li} > 0$) and blue ones unstable ($\Delta G_{LLZOM-Li} < 0$). Besides the 100 training data points, predictions were made for 18 unexplored compounds, labeled as crosses in Fig. 4. It is clear that compounds that are stable and unstable at Li|LLZOM interfaces are well separated by the black solid lines, which divide the ($\Delta H_{f,x+y}$, CN × $\Delta H_{f,x}$) and ($\Delta H_{f,x+y}$, BDE) maps into two regions with only a few exceptions. We observe that the 18 predicted data points (yellow crosses and blue crosses) are perfectly predicted by the training model, falling within the respective stable and unstable regions established by the training data. The ($\Delta H_{f,x+y}$, CN × $\Delta H_{f,y}$) and ($\Delta H_{f,x+y}$, χ_M) classification maps are also plotted in Fig. S5.† From the chemical bond point of view, since the selected features, such as ΔH_f and BDE, can be viewed as indicators of the M–O bond strength, based on our machine learning procedures it can be qualitatively concluded that the Li|LLZOM interface stability could be mainly measured by the local M–O chemical bond strength.

To quantitatively understand the Li|LLZOM interfacial thermodynamic stability, the reaction energies $\Delta G_{LLZOM-Li}$ and single

Fig. 4 Maps of (a) $\Delta H_{f,x+y}$ and CN × $\Delta H_{f,x}$, and (b) $\Delta H_{f,x+y}$ and M–O bond dissociation energy (BDE) feature pairs for 100 LLZOM compounds considered in our work. 18 unexplored data points are also predicted and plotted. Blue circles and yellow circles are the 100 training data points, and blue crosses and yellow crosses are the 18 predicted data points. The evaluation of classification performance for the SVM models involves feature pairs when both features are standard scalers. Brown and sky-blue areas represent thermodynamically stable and unstable regions, respectively.

19966 | *J. Mater. Chem. A*, 2019, **7**, 19961–19969

This journal is © The Royal Society of Chemistry 2019

Fig. 5 The dependence of the reaction energy $\Delta G_{LLZOM-Li}$ of Li|LLZOM interface on (a) $\Delta H_{f,x+y}$ and (b) M−O bond dissociation energy. The dotted boxes represent the most appropriate range for each feature.

feature ($\Delta H_{f,x+y}$, BDE) relations are plotted in Fig. 5. We observe that oxides M_xO_y with larger negative formation energies ($|\Delta H_{f,x+y}|$ > 3.5 eV) give rise to more thermodynamically stable Li|LLZOM interfaces, and the M−O BDE directly reflects the local chemical bond strength of the initial LLZOM structure stability, shown in Fig. 5a and b, respectively. The greater the BDE, the more heat needs to be absorbed to disrupt the M−O bond in LLOZM during the chemical reactions. Similarly, it is clear that the majority of stable Li|LLZOM interfaces have a large negative CN × $\Delta H_{f,y}$ value, corresponding to the local chemical bond strength. In terms of the Pauling electronegativity χ_M, the appropriate range for Li|LLZOM interface stability is between 1.0 and 1.5 with only a few exceptions, as shown in ESI Fig. S6.† Therefore, we conclude that the thermodynamic stability of the Li|LLZOM interface relates to the stronger ionic bonding nature of M−O in LLZOM, which is in agreement with the report by Nakayama.[18]

In order to quantitatively obtain a prediction model for reaction energy ΔG, the KRR algorithm (with the best performance among five algorithms, see Table S8†) was employed. The model is based on the training data (80% of the full dataset), and is used to evaluate the test data. A plot of 100 LLZOM ΔG values predicted using KRR *versus* the DFT calculated values is presented in Fig. 6. The results clearly show good agreement between the DFT values and KRR predictions, with the R^2 and MSE of the test data as 0.92 and 0.04, respectively. Then, the trained KRR model is applied to the unexplored 18 LLZOM to predict their ΔG values, and the prediction results are listed in Table S6.† We notice that the predicted 18 ΔG values are in excellent correlation with the relevant feature statistics ($|\Delta H_{f,x+y}|$ > 3.5 eV; 1.0 < χ_M < 1.5). More importantly, the reaction energies of the 18 LLZOM systems are calculated by the automated reaction calculations, confirming the prediction model. Therefore, combining machine learning technology and high-throughput automated reaction calculations, we have developed an extremely fast target-driven method to predict the reaction energies for the Li|LLZOM interface systems. This workflow can be readily applied to other solid electrolyte materials.
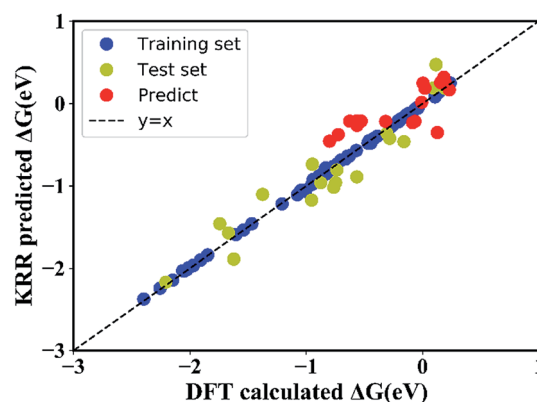

Fig. 6 DFT calculated reaction energies (ΔG) compared with the predicted reaction energies using a kernel ridge regression model. The model is trained on a randomly selected 80% training set from the 100 LLZOM database using the 15 features. The coefficient of determination (R^2) and mean squared error (MSE) are computed to estimate the prediction errors. The training and test points are show in blue and green, respectively. The perfect correlation line is included for reference as a black dashed line.

Beneficial effects of the interphase layer

Based on the automated reaction screening of the interfacial phases, an LLZOM that is unstable against Li metal would generate an interphase layer, similar to the formation of a solid electrolyte interphase (SEI) layer, as shown in Fig. 7. In fact, the interphase layer formed by the reactions also has the attribute of improving the stability of the interface, depending on the electrical conductivity of the product phases.[55] If the product phases are electrically insulating, they will form a passivated interface layer that promotes interfacial contacts and reduces the interfacial impedance.[56,57] In addition, the passivating interphase layer can prevent LLZOM from further reaction and suppress Li dendrite growth during cycling.[15,58] For example, some elements, M = Ca^{2+} (La or Zr), Yb^{3+} (La), Br^{3+} (Li), Te^{4+} (Zr), Se^{4+} (Zr), S^{4+} (Zr), Hf^{4+} (Zr), Cl^{5+} (Zr), and I^{5+} (Zr), when in equilibrium with Li metal, typically decompose into products

Fig. 7 Improvement of Li|LLZOM (M = dopants) interfacial stability *via* the formation of a passivating interface layer.

that are electrically insulating with bandgaps >2.0 eV (bandgap data from MP,[33] see Table S7†), *e.g.*, CaO, YbO, LiBr, La_2TeO_2, La_2SeO_2, La_2SO_2, $Li_6Hf_2O_7$, LiCl, and LaIO. For LLZOs with other dopants, the undesired high electrical conductivities of the interphase layers may cause continuous decomposition of the LLZOM materials, and a passivating interphase cannot be achieved at the interface.[59] In previous work, the non-passivating behavior of the interphase was confirmed, the interphase layers and the resistance increasing markedly in a short period of time.[9] Therefore, the electrical conductivity of the interphase layer is also a crucial factor in determining the interfacial stability of LLZOM against Li metal anode.

Conclusions

In this work, we have developed a high-throughput automated reaction screening and machine learning approach to evaluate possible reactions and the thermodynamic stability of Li|LL-ZOM interfaces under various chemical conditions. Our calculations reveal that LLZOM stability against Li metal is governed by the dopants. We discover that M = Sc^{3+} (Zr), Ce^{3+} (Zr or La), Ac^{3+} (La), Y^{3+} (La or Zr), Tm^{3+} (La or Zr), Er^{3+} (La or Zr), Ho^{3+} (La or Zr), Dy^{3+} (La or Zr), Nd^{3+} (La or Zr), Tb^{3+} (La or Zr), Pr^{3+} (La), Pm^{3+} (La or Zr), Sm^{3+} (La or Zr), Gd^{3+} (La or Zr), Lu^{3+} (La), Ce^{4+} (Zr), Th^{4+} (Zr), Pa^{5+} (Zr), Ca^{2+} (La or Zr), Yb^{3+} (La), Br^{3+} (Li), Te^{4+} (Zr), Se^{4+} (Zr), S^{4+} (Zr), Hf^{4+} (Zr), Cl^{5+} (Zr), and I^{5+} (Zr) exhibit stability against Li metal, either because the interface is thermodynamically stable or as a result of stable passivation. However, LLZOMs with other dopant cations are likely reduced by Li metal, while passivating interphases cannot be achieved at the interface. On the basis of a large amount of data, we have attempted to find the underlying physical mechanisms of the thermodynamic stability of Li|LLZOM interfaces by employing a machine learning technique. Based on our analysis, the stability of the Li|LLZOM interface is determined by the M–O chemical bond strength. Our results provide a guiding principle for selecting cation doping in LLZO to provide stability against Li metal, and show the potential for the fast screening of new LLZOM materials by the machine learning approach.

Conflicts of interest

The authors declare that there are no conflicts of interest.

Acknowledgements

References

1 W. Xu, J. Wang, F. Ding, X. Chen, E. Nasybulin, Y. Zhang and J.-G. Zhang, *Energy Environ. Sci.*, 2014, **7**, 513–537.

2 D. Lin, Y. Liu and Y. Cui, *Nat. Nanotechnol.*, 2017, **12**, 194.

3 B. Liu, J.-G. Zhang and W. Xu, *Joule*, 2018, **2**, 833–845.

4 X.-B. Cheng, R. Zhang, C.-Z. Zhao and Q. Zhang, *Chem. Rev.*, 2017, **117**, 10403–10473.

5 X. Q. Zhang, X. B. Cheng and Q. Zhang, *Adv. Mater. Interfaces*, 2018, **5**, 1701097.

6 H. Duan, H. Zheng, Y. Zhou, B. Xu and H. Liu, *Solid State Ionics*, 2018, **318**, 45–53.

7 F. Han, J. Yue, C. Chen, N. Zhao, X. Fan, Z. Ma, T. Gao, F. Wang, X. Guo and C. Wang, *Joule*, 2018, **2**, 497–508.

8 A. Wang, S. Kadam, H. Li, S. Shi and Y. Qi, *npj Comput. Mater.*, 2018, **4**, 15.

9 S. Wenzel, S. Randau, T. Leichtweiß, D. A. Weber, J. Sann, W. G. Zeier and J. Janek, *Chem. Mater.*, 2016, **28**, 2400–2407.

10 S. Wenzel, D. A. Weber, T. Leichtweiss, M. R. Busche, J. Sann and J. Janek, *Solid State Ionics*, 2016, **286**, 24–33.

11 A. Schwöbel, R. Hausbrand and W. Jaegermann, *Solid State Ionics*, 2015, **273**, 51–54.

12 S. Stramare, V. Thangadurai and W. Weppner, *Chem. Mater.*, 2003, **15**, 3974–3990.

13 H. Aono, E. Sugimoto, Y. Sadaoka, N. Imanaka and G. y. Adachi, *J. Electrochem. Soc.*, 1990, **137**, 1023–1027.

14 Y. Li, W. Zhou, X. Chen, X. Lü, Z. Cui, S. Xin, L. Xue, Q. Jia and J. B. Goodenough, *Proc. Natl. Acad. Sci. U. S. A.*, 2016, **113**, 13313–13317.

15 B. Wu, S. Wang, J. Lochala, D. Desrochers, B. Liu, W. Zhang, J. Yang and J. Xiao, *Energy Environ. Sci.*, 2018, **11**, 1803–1810.

16 M. Ramaswamy, T. Venkataraman and W. Werner, *Angew. Chem., Int. Ed.*, 2007, **46**, 7778–7781.

17 M. Kotobuki, H. Munakata, K. Kanamura, Y. Sato and T. Yoshida, *J. Electrochem. Soc.*, 2010, **157**, A1076–A1079.

18 M. Nakayama, M. Kotobuki, H. Munakata, M. Nogami and K. Kanamura, *Phys. Chem. Chem. Phys.*, 2012, **14**, 10008–10014.

19 T. Thompson, S. Yu, L. Williams, R. D. Schmidt, R. Garcia-Mendez, J. Wolfenstine, J. L. Allen, E. Kioupakis, D. J. Siegel and J. Sakamoto, *ACS Energy Lett.*, 2017, **2**, 462–468.

20 S. Ohta, T. Kobayashi and T. Asaoka, *J. Power Sources*, 2011, **196**, 3342–3345.

21 H. Buschmann, S. Berendts, B. Mogwitz and J. Janek, *J. Power Sources*, 2012, **206**, 236–244.

22 P. Bottke, D. Rettenwander, W. Schmidt, G. Amthauer and M. Wilkening, *Chem. Mater.*, 2015, **27**, 6571–6582.

23 Y. Li, Z. Wang, Y. Cao, F. Du, C. Chen, Z. Cui and X. Guo, *Electrochim. Acta*, 2015, **180**, 37–42.

24 J. Wolfenstine, J. Ratchford, E. Rangasamy, J. Sakamoto and J. L. Allen, *Mater. Chem. Phys.*, 2012, **134**, 571–575.

25 D. Rettenwander, P. Blaha, R. Laskowski, K. Schwarz, P. Bottke, M. Wilkening, C. A. Geiger and G. Amthauer, *Chem. Mater.*, 2014, **26**, 2617–2623.

26 H. Nemori, Y. Matsuda, S. Mitsuoka, M. Matsui, O. Yamamoto, Y. Takeda and N. Imanishi, *Solid State Ionics*, 2015, **282**, 7–12.

27 Y. Kim, A. Yoo, R. D. Schmidt, A. Sharafi, H. Lee, J. Wolfenstine and J. Sakamoto, *Front. Energy Res.*, 2016, **4**, 1–7.

28 C. Ma, Y. Cheng, K. Yin, J. Luo, A. Sharafi, J. Sakamoto, J. Li, K. L. More, N. J. Dudney and M. Chi, *Nano Lett.*, 2016, **16**, 7030–7036.

29 D. Rettenwander, R. Wagner, A. Reyer, M. Bonta, L. Cheng, M. M. Doeff, A. Limbeck, M. Wilkening and G. Amthauer, *J. Phys. Chem. C*, 2018, **122**, 3780–3785.

30 J. G. Connell, Y. Zhu, P. Zapol, S. Tepavcevic, A. Sharafi, J. Sakamoto, L. A. Curtiss, D. D. Fong, J. W. Freeland and N. M. Markovic, *ACS Appl. Mater. Interfaces*, 2018, **10**, 17471–17479.

31 Y. Zhu, J. G. Connell, S. Tepavcevic, P. Zapol, R. Garcia-Mendez, N. J. Taylor, J. Sakamoto, B. J. Ingram, L. A. Curtiss, J. W. Freeland, D. D. Fong and N. M. Markovic, *Adv. Energy Mater.*, 2019, **9**, 1803440.

32 S. Kirklin, J. E. Saal, B. Meredig, A. Thompson, J. W. Doak, M. Aykol, S. Rühl and C. Wolverton, *npj Comput. Mater.*, 2015, **1**, 15010.

33 S. P. Ong, W. D. Richards, A. Jain, G. Hautier, M. Kocher, S. Cholia, D. Gunter, V. L. Chevrier, K. A. Persson and G. Ceder, *Comput. Mater. Sci.*, 2013, **68**, 314–319.

34 K. B. John, P. Perdew and M. Ernzerhof, *Phys. Rev. Lett.*, 1996, **77**, 3865–3868.

35 G. Kresse, *Phys. Rev. B*, 1999, **59**, 1758–1775.

36 G. Kresse, *Phys. Rev. B*, 1996, **54**, 11169–11186.

37 P. P. Ewald, *Ann. Phys.*, 1921, **369**, 253–287.

38 P. Nash, https://tptc.iit.edu/index.php/thermo-database, 2013.

39 L. f. T. Hüttenkunde and R.-W. T. H. Aachen, *Thermodynamic Properties of Inorganic Materials, Landolt-Börnstein, New Series*, 1999, vol. 19.

40 B. He and S. Shi, *Screening platform for solid electrolyte*, Shanghai University, 2018, https://www.bmaterials.cn.

41 R. Xiao, H. Li and L. Chen, *Sci. Rep.*, 2015, **5**, 14227.

42 L. Pan, L. Zhang, A. Ye, S. Chi, Z. Zou, B. He, L. Chen, Q. Zhao, D. Wang and S. Shi, *J. Materiomics*, 2019, DOI: 10.1016/j.jmat.2019.04.010.

43 G. Pilania, P. V. Balachandran, C. Kim and T. Lookman, *Front. Mater.*, 2016, **3**, 1–7.

44 S. Shi, J. Gao, Y. Liu, Y. Zhao, Q. Wu, W. Ju, C. Ouyang and R. Xiao, *Chin. Phys. B*, 2016, **25**(1), 018212.

45 Y. Liu, T. Zhao, W. Ju and S. Shi, *J. Materiomics*, 2017, **3**, 159–177.

46 J. Schmidt, J. Shi, P. Borlido, L. Chen, S. Botti and M. A. L. Marques, *Chem. Mater.*, 2017, **29**, 5090–5103.

47 Y. Wang, W. Zhang, L. Chen, S. Shi and J. Liu, *Sci. Technol. Adv. Mater.*, 2017, **18**, 134–146.

48 W. Li, R. Jacobs and D. Morgan, *Comput. Mater. Sci.*, 2018, **150**, 454–463.

49 S. Lu, Q. Zhou, Y. Ouyang, Y. Guo, Q. Li and J. Wang, *Nat. Commun.*, 2018, **9**, 3405.

50 L. J. Miara, W. D. Richards, Y. E. Wang and G. Ceder, *Chem. Mater.*, 2015, **27**, 4040–4047.

51 A. O. Oliynyk, E. Antono, T. D. Sparks, L. Ghadbeigi, M. W. Gaultois, B. Meredig and A. Mar, *Chem. Mater.*, 2016, **28**, 7324–7331.

52 R. Shannon, *Acta Crystallogr., Sect. A: Cryst. Phys., Diffr., Theor. Gen. Crystallogr.*, 1976, **32**, 751–767.

53 Y. R. Luo, *Comprehensive Handbook of Chemical Bond Energies*, CRC Press, Boca Raton, FL, 2007.

54 F. Pedregosa, G. Varoquaux, A. Gramfort, V. Michel, B. Thirion, O. Grisel, M. Blondel, P. Prettenhofer, R. Weiss, V. Dubourg, J. Vanderplas, A. Passos, D. Cournapeau, M. Brucher, M. Perrot and E. Duchesnay, *J. Mach. Learn. Res.*, 2011, **12**, 2825–2830.

55 Y. Shen, Y. Zhang, S. Han, J. Wang, Z. Peng and L. Chen, *Joule*, 2018, **2**, 1674–1689.

56 X. Han, Y. Gong, K. Fu, X. He, G. T. Hitz, J. Dai, A. Pearse, B. Liu, H. Wang, G. Rubloff, Y. Mo, V. Thangadurai, E. D. Wachsman and L. Hu, *Nat. Mater.*, 2016, **16**, 572.

57 K. Fu, Y. Gong, B. Liu, Y. Zhu, S. Xu, Y. Yao, W. Luo, C. Wang, S. D. Lacey, J. Dai, Y. Chen, Y. Mo, E. Wachsman and L. Hu, *Sci. Adv.*, 2017, **3**, e1601659.

58 Z. Zhang, L. Zhang, Y. Liu, H. Wang, C. Yu, H. Zeng, L.-m. Wang and B. Xu, *ChemSusChem*, 2018, **11**, 3774–3782.

59 Y. Z. Zhu, X. F. He and Y. F. Mo, *Adv. Sci.*, 2017, **4**, 1600517.

This journal is © The Royal Society of Chemistry 2019

J. Mater. Chem. A, 2019, **7**, 19961–19969 | **19969**